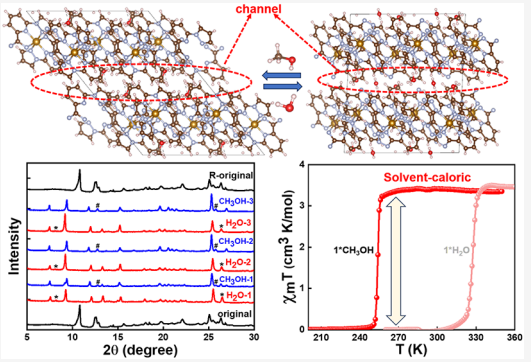
JACS
JOURNAL OF THE AMERICAN CHEMICAL SOCIETY
pubs.acs.org/JACS
Article

Colossal and Reversible Barocaloric and Solvent-Caloric Effects in a T_C-Adjustable Spin-Crossover Complex

Yue Kan,[##] Si-Wei Yan,[##] Shuo Meng,[##] Yuan Lin, Rui-Xin Li, Qing-Zhen Huang, Yue-Xing Zhang, Zheng-Ying Tian, Jing Wang, Yuan-Sha Chen, Yun-Zhong Chen, Ji-Rong Sun, Dao-Peng Zhang,* Chang-Qing Jin, Feng-Xia Hu,* and Bao-Gen Shen*

Cite This: *J. Am. Chem. Soc.* 2026, 148, 35916−35928
Read Online
ACCESS | Metrics & More | Article Recommendations | Supporting Information

ABSTRACT: Barocaloric effects (BCE) represent an appealing refrigeration technology and have attracted great interest recently. However, most BCE materials still cannot meet real-world refrigeration requirements because of their fixed phase transition temperature T_C and the significantly high pressure required to drive a wide cooling temperature span. Here, we address these bottlenecks by engineering molecular channels in a SCO complex, Fe[L_2]. Besides the observation of colossal and reversible BCE in Fe[L_2], the designed molecular channels allow fast commutation of H_2O and CH_3OH, which enables the tunability of T_C and creates a refrigeration window as wide as 80 K by simply altering the solvent atmosphere, as confirmed by SC-XRD, P-DSC, PXRD, Raman, and DFT calculations. Inspired by the proposed "solvent-caloric" effect, the refrigeration capacity at ambient pressure can be 9 times higher than that achieved at 100 MPa using conventional BCE methods, greatly boosting the universality for different BCE refrigeration scenarios. Our results demonstrate that the designed molecular channels in SCO complexes can influence the SCO transition properties and thereby bring forth singular caloric phenomena, offering new routes for orchestrating novel cooling materials.



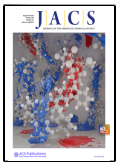
INTRODUCTION

Refrigeration can be found everywhere, and it is used in almost all fields; nearly 25% of global electricity is consumed by this sector.[1] In addition, with inexorable development, the demand for cooling is predicted to further increase at a drastic speed in the next few decades.[2] For example, the energy required for in-house refrigeration is likely to triple by 2050.[3] However, the main refrigerants used nowadays in cooling technology are still volatile hydrofluorocarbon (HFC)-based on the vapor-compression cycle, whose global warming potentials (GWPs) can be 2000 times higher than those of common CO_2—a real alarming crisis in terms of greenhouse gas emissions due to the potential leakage of these refrigerants.[4,5] Therefore, it is exigent to create new cooling technologies that eliminate GWP.

Solid-state cooling based on caloric effects has a compelling capability to undertake such an arduous task.[6−21] Particularly, the past few years have witnessed the thriving of the barocaloric effect (BCE).[6−8,22,23] The finding of a colossal BCE material in the plastic crystal NPG, with a colossal entropy change of more than 500 J K^{-1} kg^{-1} from the orientational order−disorder transition in 2019, is a milestone and has strongly boosted research in this field.[8,9] Latterly, a brand-new colossal BCE was found in ionic plastic crystals,[12] and an extreme BCE was recently reported in NH_4SCN solutions through pressure-driven dissolution and precipitation.[10] Although many samples have been reported for BCE applications with a colossal entropy change of more than 100 J K^{-1} kg^{-1},[6−8,11,22,23] the real-world performance is still in doubt. One bottleneck lies in the fact that the working/cooling temperature span under a certain pressure is always limited around their own transition temperature T_C, and typically, the effective refrigeration temperature span is always below 25 K even under a pressure of 100 MPa (Table 1).[7−9,19] Thus, it is difficult to satisfy various cooling scenarios with different refrigeration windows as well as a relatively large temperature span, whose driving pressure is also a concern in terms of practicality.

Decades of foundational research on spin crossover (SCO) molecule materials have yielded a deep understanding of mechanisms and a diverse chemical library, and the community is now shifting toward application-driven design. Hexa-coordinated (pseudo-)octahedral Fe^{II} complexes, as the most renowned members of the SCO family, can reversibly change

Received: May 11, 2026
Revised: July 25, 2026
Accepted: July 28, 2026
Published: August 13, 2026



Downloaded from pubs.acs.org/jacsat/article-pdf/148/33/35916/6653044/jacs.6c09635.pdf by INST OF PHYSICS user on 06 September 2026

© 2026 American Chemical Society

Table 1. Refrigeration Span for Some Representative BCE Materials[a]

	Compound	T_C at 0 MPa (K)	T_C at 100 MPa (K)	Temperature span at 100 MPa (K)	dT_C/dP (K/MPa)	Ref.
Organic	$C_{16}H_{34}$	291	316	25	0.25	7
	$C_{18}H_{38}$	305	325	20	0.2	7
	Para-carborane	308	346	38	0.38	52
	NPG	320	333	13	0.13	8,9
	$[N_{2222}][TFSI]$	278	301.7	23.7	0.237	19
	PG	354	363.4	9.4	0.094	44
	NPA	232	254	22	0.22	44
	TRIS	407	410.7	3.7	0.037	44
	AMP	352	360.5	8.5	0.085	44
	PEG10000/PET15000	334.6	344.3	9.7	0.097	22
	$(C_9H_{19}NH_3)_2MnCl_4$	295	312.2	17.2	0.172	23
	$(C_{10}H_{21}NH_3)_2MnCl_4$	315	333	18	0.18	23
Inorganic	$Fe[HB(tz)_3]_2$	333	355	22	0.22	20
	$Fe(L)(NCS)_2$	270	298.4	19.4	0.194	21
	$Fe_3(bntrz)_6(tcnset)_6$	318	343	25	0.25	13
	$[TPrA][Mn(dca)_3]$	331	354.1	23.1	0.231	45
	$C_7H_{14}NReO_4$	344	357.8	13.8	0.138	46
	$[Cp_2Fe][PF_6]$	347	381.1	34.1	0.341	47
	$MnCoGeB_{0.03}$	298	288	10	−0.1	48
	AgI	430	406	24	−0.24	49
	$(NH_4)_2SO_4$	219	223.5	4.5	0.045	50
	C_{60}	260	277.2	17.2	0.172	51
	NH_4I	273	280.9	7.9	0.79	53
	1	**293**	**308**	**15**	**0.15**	**This work**
	1*CH_3OH/1*H_2O-commutation	**240 1*H_2O**	**320 1*CH_3OH**	**80***	-	**This work**

[a]Temperature span driven by the commutation of CH_3OH and H_2O in this work.

between the high-spin (HS, $t_{2g}^4e_g^2$) and low-spin (LS, $t_{2g}^6e_g^0$) states under external stimuli such as temperature, pressure, electric/magnetic fields, light irradiation, and guest molecules, among others (Figure S1). By companying the dramatic changes in color, optical, magnetic, mechanical, dielectric, and structural properties, this bistability confers great potential on SCO materials for use in molecular electronics, sensing, data storage, mechanical transducers, and displays. Yet, the limited number of systems that can be precisely tailored to meet the specific property profiles required for different technologies makes the application of SCO materials still challenging, even though the external factors listed above can be used to tune SCO functional properties , such as spin transition temperature, thermal hysteresis width, and light-induced excited spin state trapping (LIESST), etc. The transformation between LS (S = 0) and HS (S = 2), originating from the splitting of the 3d orbital of the Fe^{II} ions, creates a significant entropy change as well as considerable lattice expansion/contraction (1−10%) due to the changeable coordination geometry of the metal ion,[13−15,20,21] implying the potential mechanocaloric cooling function of these types of compounds. In 2016, the SCO transition was first proposed as a feasible mechanism to induce the barocaloric effect,[12] and the BCE of a few Fe^{II}-based SCO complexes has been investigated with pressure being the unique factor to tune refrigeration performance over the past 10 years, strongly suggesting the practical application value of SCO materials in the mechanical refrigeration field. Owing to the rich chemical configurations and operability of SCO complexes,[18,24−26] pores or even molecular channels can be designed in the cell structure, allowing adsorption/desorption of external solvent molecules, and hence significant changes in the ligand field around central metal ions can occur. The caloric effect of solvation/desolvation, happening without the application of pressure to achieve refrigeration, has not been explored to date in reported SCO research, although the cocrystallized solvent content has been proven to have an obvious influence on the SCO transition temperature T_C. Exploring the chemical reaction potential for refrigeration, rather than relying on external work, could usher in a new paradigm in cooling technology.

Herein, we researched a SCO complex, $[Fe(L)_2]$ (chemical formula: $C_{18}H_{12}FeN_{14}$, L = (2-(1H-pyrazol-1-yl)-6-(1H-tetrazol-5-yl)pyridine), denoted as **1** for simplicity) on the barocaloric effect, where molecular channels were designed to allow external solvents (H_2O, CH_3OH) to enter and exit, accompanying an interesting "solvent-caloric" effect for tuning the spin transition temperature and thereby adjusting the refrigeration performance. The intrinsic structure was revealed via single-crystal and powder X-ray diffraction (SC-XRD, PXRD), and the thermal properties were explored by commercial Pressure-Differential Scanning Calorimetry (P-DSC). Solvent-influenced T_C was clarified by magnetic measurements using a Superconducting Quantum Interference Device (SQUID), which confirmed the adjustability of T_C by alternating the solvent molecules in the crystal lattice, and the potential refrigeration window was enlarged to ∼80 K. The mechanism behind this was explained via density functional theory (DFT) in terms of complexation energy and accessible solvent surface. On this basis, a new refrigeration caloric method based on the solvent-caloric effect was proposed in terms of driving the phase transition and the cooling cycle by adjusting the solvent atmosphere besides the traditional pressure.

Downloaded from pubs.acs.org/jacsat/article-pdf/148/33/35916/6653044/jacs.6c09635.pdf by INST OF PHYSICS user on 06 September 2026

https://doi.org/10.1021/jacs.6c09635
J. Am. Chem. Soc. 2026, 148, 35916−35928

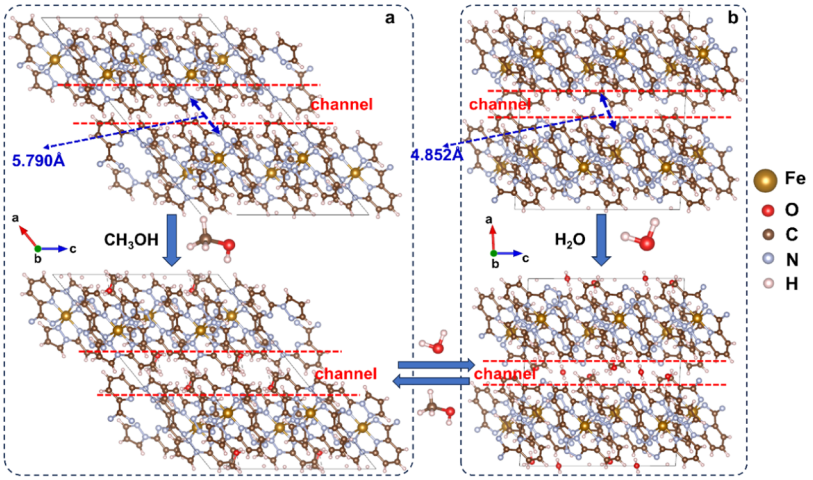


Figure 1. The 3D structure of (a) **1*CH$_3$OH** and (b) **1*H$_2$O** obtained from SC-XRD. The channels in the structure are illustrated with dashed lines, where the external solvent molecules can enter the cell structure as presented. The accurate number of solvent molecules in the lattice was determined to be 1 and 1.5 for CH_3OH and H_2O, respectively. The channel width along the *a*-axis is measured by the distance between (a) the N2 atom of the pyrazole ring in the ligand on the upper side of the channel and the N2 atom of the pyrazole ring in the ligand on the lower side of the channel; (b) the C2 atom of the pyridine ring on the upper side of the channel and the C5 atom of the tetrazole ring in the ligand on the lower side of the channel.

RESULTS AND DISCUSSION

Yellow-orange single crystals of **1*CH$_3$OH** with molecular channels were synthesized by the solvent method; see details provided in the Methods section in the Supporting Information. After placing the sample in air for 1−2 min, the color of **1*CH$_3$OH** changed to red-orange, as shown in Figure S8. This is because the solvent molecules in the crystal lattice were replaced from CH_3OH to H_2O (**1*H$_2$O**, *vide infra*). The red-orange single crystals further changed to dark orange powder after thermal treatment at 40 °C for 4 h, during which the H_2O molecules completely evaporated from the lattice. The resulting solvate-free sample, namely **1**, is stable in air. Our measurements of temperature-dependent magnetic susceptibility validated the SCO nature for both **1** and its derivatives. For **1**, the T_C of SCO, defined as the temperature where the $\chi_m T$ value is half of the maximum, was determined to be 295 K for heating and 293 K for cooling, respectively, with a small thermal hysteresis of 2 K. As for **1*CH$_3$OH** and **1*H$_2$O**, the sharp SCO transition remains the same as that of **1**, except for the conspicuous shift of T_C, with ∼250 K for **1*CH$_3$OH** and ∼325 K for **1*H$_2$O**, while the thermal hysteresis remains similarly small, ∼2 K.

Formation of Molecule Channels

The lattice structure of polycrystalline powder **1**, measured by PXRD at room temperature and refined via the Le Bail method, is monoclinic with a *P2/m* space group (Tables S3 and S4). Its lattice parameters are a = 19.416(2) Å, b = 14.103(1) Å, c = 14.003(1) Å, $\alpha = \gamma = 90°$, and β = 121.747(5)°. Although the accurate structure of **1**, without any solvent molecules, was not obtained due to the poor single-crystal quality of **1**, it can be inferred that the overall structure of **1** is similar to its derivatives according to the intrinsic properties of these kinds of SCO complexes.[26−30] Based on the structural information for **1*CH$_3$OH** and **1*H$_2$O** obtained by SC-XRD (Figure 1), it is reasonable to say that the asymmetric unit of **1** is a typical mononuclear structure with the Fe(II) ion located at the center and connected to six N atoms from two chelating tridentate ligands (Figure S2). The entire systematic 3D network is formed by the linkage of numerous individual asymmetric units with the help of H-bond interactions of C−H···N and π-π stacking interactions, including the π-stacking between two pyrazolyl units, and the edge-to-face π-stacking between a pyrazolyl ring and a tetrazolyl ring.

For the structure of single crystals **1*CH$_3$OH** and **1*H$_2$O** analyzed by SC-XRD, the most distinct characteristic for them is the remarkable channels formed throughout the bodies, as highlighted by red dashed lines in Figure 1, which are not common in most SCO complexes. The widths of these channels are ∼5.790 Å and ∼4.852 Å in **1*CH$_3$OH** and **1*H$_2$O**, respectively, as marked by blue dashed arrows, which are large enough to accommodate CH_3OH (∼1.306 Å) and H_2O (∼1.232 Å) molecules. Therefore, CH_3OH as well as H_2O can easily reside therein, as revealed by SC-XRD. After the entrance of CH_3OH or H_2O, the initial structure of **1** transforms into *C2/c* and *I2/a* for **1*CH$_3$OH** and **1*H$_2$O**, respectively (Tables S1 and S2). Note that the space groups of all three (**1**, **1*CH$_3$OH** and **1*H$_2$O**) belong to the same point group *2/m*, which indicates that the entrance of external solvents does not change the whole structure significantly, i.e., only distortion of molecular skeletons.

Moreover, the formed channels are long enough to connect the unit cell from one to the other; thus, the external solvent molecules can enter or leave, as illustrated by the concrete arrows in Figure 1. The small complexation energy makes the molecules easily replaceable when other molecules overwhelm the ones originally existing in the channel (see DFT calculation below, Table 1 and Movie S1), bringing forth the novel replacement between **1*H$_2$O** and **1*CH$_3$OH**. The transformation would induce a considerable change in the ligand field felt by the central Fe(II) ions,[29,31−33] hence leading to a significant shift in T_C. As a result, the commonly limited refrigeration temperature span (<25 K) (Table 1) for BCE materials, even under high pressure above 100 MPa, can be significantly mediated with the help of this commutation.

Spin-Crossover-Induced Structural Change and Dynamics

The derivatives of **1** (**1*H$_2$O** and **1*CH$_3$OH**) behave unstably in air since the inherent channels formed therein are extremely

Downloaded from pubs.acs.org/jacsat/article-pdf/148/33/35916/6653044/jacs.6c09635.pdf by INST OF PHYSICS user on 06 September 2026

https://doi.org/10.1021/jacs.6c09635
J. Am. Chem. Soc. 2026, 148, 35916−35928

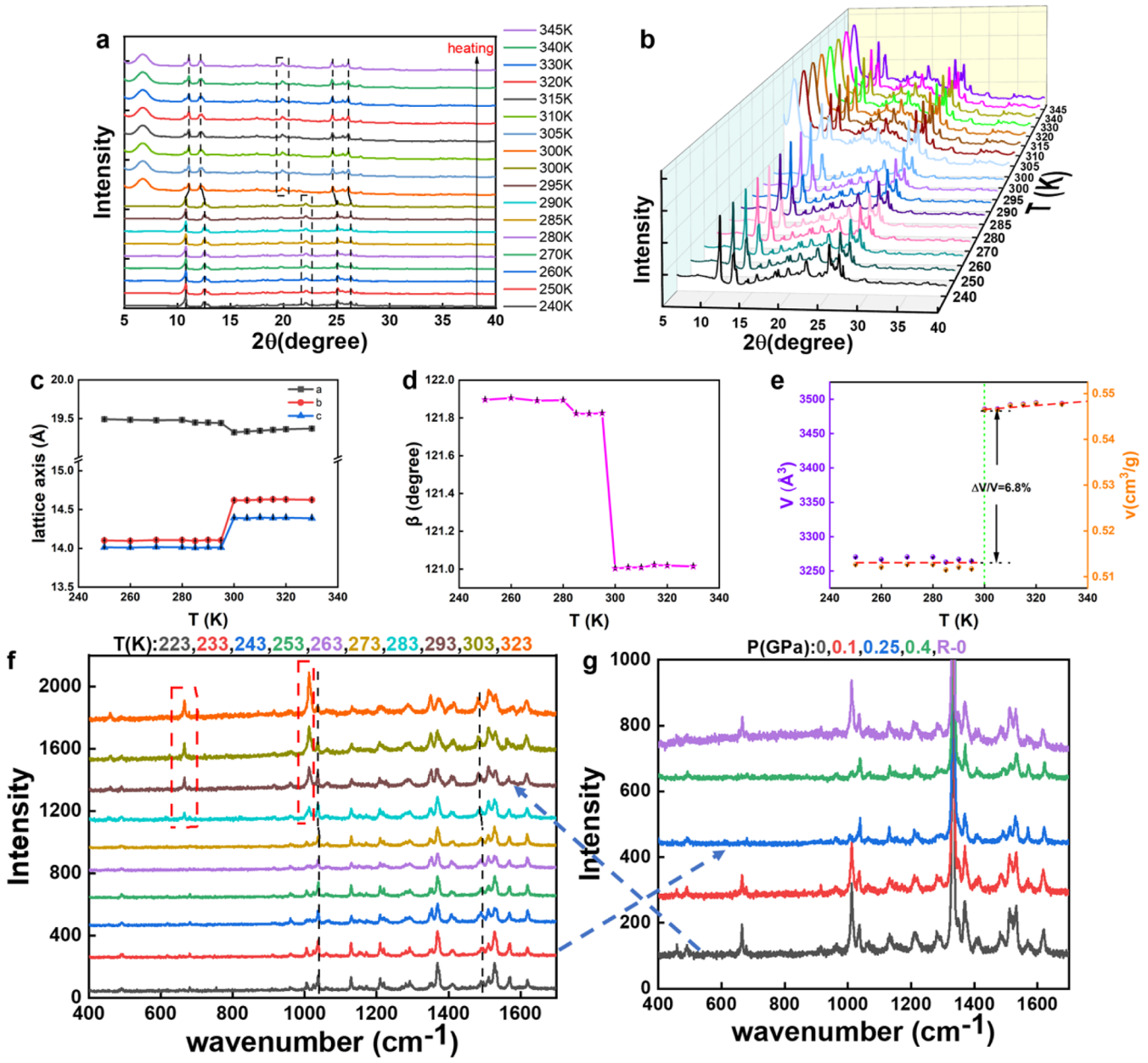


Figure 2. VT-PXRD and VT/VP-Raman of 1. (a) Raw data of XRD on heating from 240 to 345 K (the large swell at 6.7° above 300 K originates from the high-temperature sample holder), (b) 3D waterfall plot of (a). (c) The evolution of the lattice axes *a*, *b*, and *c* with temperature. (d) The evolution of the β angle with temperature. (e) The evolution of lattice cell volume (left axis) and the specific volume (right axis) with temperature, with the lines serving as guides for the eyes . (f) VT-Raman on heating from 223 to 323 K (T_C is slightly lower compared to other measurements due to the thermal effect caused by the laser beam). (g) VP-Raman from 0 to 0.4 GPa at room temperature and during the removal of pressure.

sensitive to water. To elucidate spin-crossover-induced structural changes and dynamics, we chose sample **1** and performed variable-temperature powder XRD (VT-PXRD) and Raman (VT-Raman) measurements. As shown in Figure 2a, the overall difference between HS and LS was not large (with the same *P2/m* space group via Le Bail refinement for both HS and LS), a typical trait for the family of 0D SCO complexes.[26,34−36] However, some diffraction peaks shifted their locations from LS to HS. The most intense peak (200) at 10.79° in LS shifted to 11.08° in HS, while a converse movement was seen for the second most intense peaks , which are also neighbors of the (200) peak, (020) and (−102), moving from 12.61° in LS to 12.10° after entering HS. In the high-angle region, a pair of peaks located around 25°−26° also both shifted from 25.09°/26.35° in LS to 24.58°/26.10° in HS, all indicating changes in lattice parameters during the SCO transition (Figure 2c,d), with axes *b* and *c* increasing while axis *a* and the β angle decreased, collectively leading to a volume expansion of $\Delta V/V \sim 6.8\%$ across the spin-state transition from LS to HS (Figure 2e), which is the source of the lattice entropy change contributing to BCE. In addition to the peaks' movements, the intensity of some peaks also changed significantly. For instance, the weak peak at 19.88° in LS became distinguishable across the SCO transition, while the opposite occurred for the peak at 22.12° in LS, which was nearly erased after the phase transition. Such phenomena inferred that the positions of individual atoms in the lattice shift due to the spin-crossover transition.

https://doi.org/10.1021/jacs.6c09635
J. Am. Chem. Soc. 2026, 148, 35916−35928

Downloaded from pubs.acs.org/jacsat/article-pdf/148/33/35916/6653044/jacs.6c09635.pdf by INST OF PHYSICS user on 06 September 2026

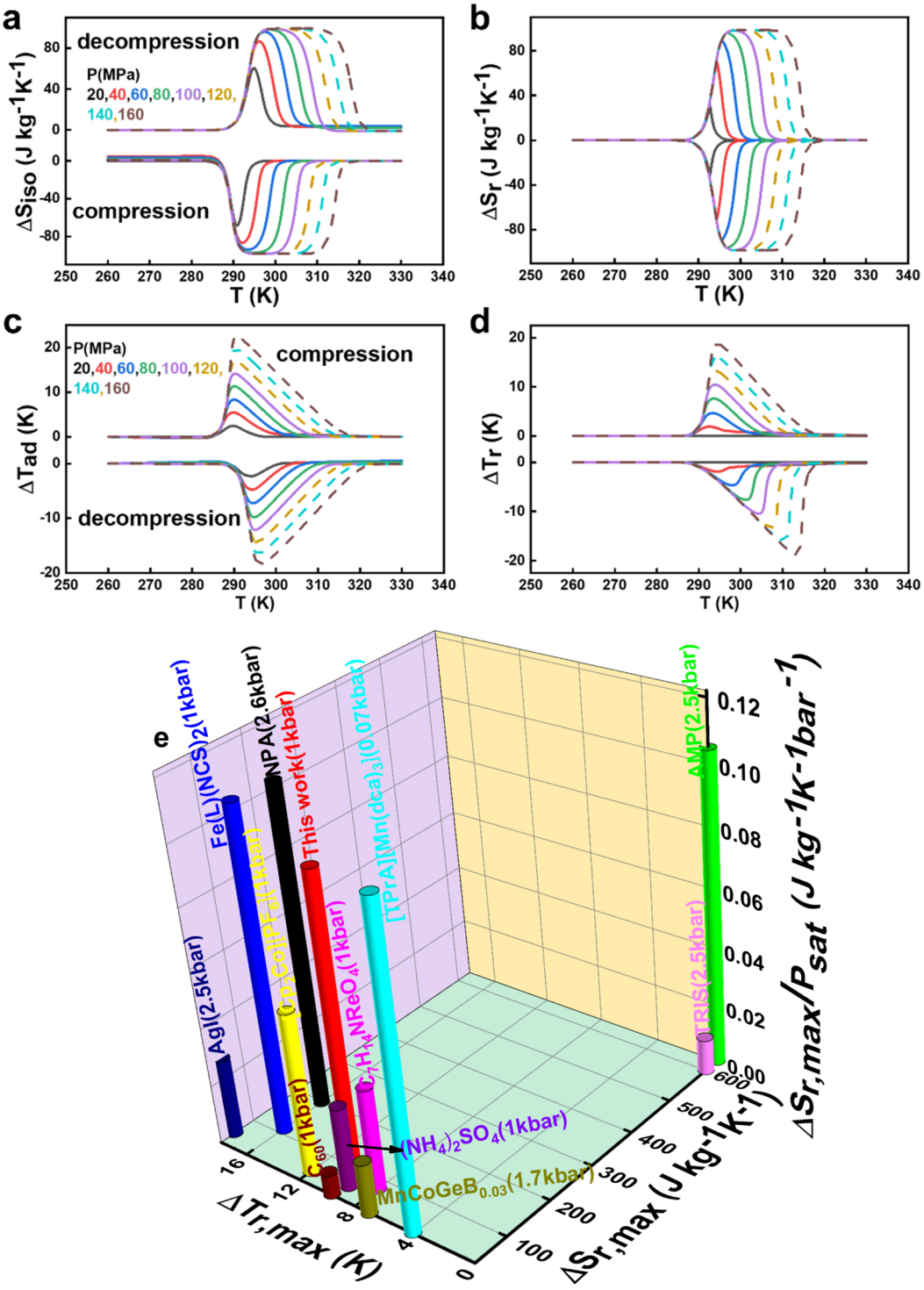


Figure 3. Barocaloric performance of 1 acquired from the P-DSC via the quasi-direct method. (a) Isothermal entropy change ΔS_{iso} at variable pressure obtained from the heat flow curves (Figure S3a) and pressure-variable entropy change curves (Figure S4). (b) Reversible entropy change ΔS_r via overlapping the compression and depressurization data from (a). (c) Adiabatic temperature change ΔT_{ad} attained through pressure-dependent entropy curves, including the contribution of specific heat (Figure S5). (d) Reversible adiabatic temperature change ΔT_r from heating entropy curve at atmospheric pressure and the cooling ones under external pressure. (e) A comparison of 1 with some representative BCE materials in terms of maximal reversible $\Delta T_{r,max}$, maximal reversible $\Delta S_{r,max}$, and the barocaloric strength $\Delta S_{r,max}/P_{sat}$, where P_{sat} is the minimal pressure required to obtain $\Delta S_{r,max}$. The values in brackets indicate the $\Delta T_{r,max}$ obtained under this pressure. For example, in the present work, (1 kbar) means that the $\Delta T_{r,max}$ of 10.4 K for 1 was induced under 1 kbar, and accurate data can be found in Table S6. The materials include organic plastic crystals $(NH_2)C(CH_2OH)_3$ (TRIS), $(NH_2)(CH_3)C(CH_2OH)_2$ (AMP), and $(CH_3)_3C(CH_2OH)$ (NPA);[44] the organic−inorganic hybrid materials $[TPrA][Mn(dca)_3]$,[45] $C_7H_{14}NReO_4$[46] and $[Cp_2Co][PF_6]$;[47] spin-crossover material $Fe(L)(NCS)_2$[21]; as well as inorganic materials $MnCoGeB_{0.03}$,[48] AgI,[49] $(NH_4)_2SO_4$,[50] and C_{60}.[51]

https://doi.org/10.1021/jacs.6c09635
J. Am. Chem. Soc. 2026, 148, 35916−35928

Downloaded from pubs.acs.org/jacsat/article-pdf/148/33/35916/6653044/jacs.6c09635.pdf by INST OF PHYSICS user on 06 September 2026

In a bid to explore the dynamics during the SCO transition, we measured variable temperature (VT) and variable pressure (VP) Raman spectroscopy (VT/VP-Raman) to reveal the evolution from the perspectives of atomic bonds' dynamics, and the outcomes are illustrated in Figure 2f,g. In line with VT-PXRD, some conspicuous changes can be distinguished. For example, the peak at 666 cm^{-1} belonging to the pyrazolyl ring in-plane bending δ-ring mode,[37−39] also the diagnostic band of **1**,[26] was nearly null at LS but became quite intense after trespassing into the HS beginning from 283 K and progressively increased with temperature (T_C in the Raman experiment is a little lower compared with other measurements due to the thermal effect caused by the laser beam). The same phenomenon was also observed for the one located at 1012 cm^{-1} ascribing to the pyrazine ring stretching υ-ring band,[37−39] as marked by the two red rectangles in Figure 2f. Besides, some peaks also shifted between the two phases, such as the one at 1040 cm^{-1} slightly red-shifting to 1036 cm^{-1} and the one in the high wavenumber region 1490 cm^{-1} also red-shifting to 1480 cm^{-1} from LS to HS. These changes indicate that the local coordination environment, molecular geometry, and intermolecular interactions are modified during the SCO transition, resulting in a reorganization of the molecular vibrations and lattice structure. The observed spectral changes should therefore be regarded primarily as Raman fingerprints of the structural and vibrational reorganization accompanying the SCO transition, rather than as direct evidence of the specific vibrational modes that dominate the transition entropy. The entropy change in SCO materials generally involves coupled electronic, spin, structural, and vibrational contributions, while low-frequency collective lattice modes are expected to play an important role in the vibrational entropy and free-energy changes associated with the transition.[40−43]

After testing the temperature influence on phase transition, we further performed VP-Raman using a diamond anvil cell (DAC) at room temperature to check the effect of pressure on **1** (Figure 2g). Before applying pressure in the DAC, the spectrum was the same as that detected in the HS (Figure 2f), indicating the original HS nature. As the pressure was applied gradually, the spectrum changed with pressure and finally transformed to the LS region at a pressure of 0.25 GPa, where the spectrum is congruent with the ones of LS in the VT experiment, as guided by the blue dashed arrows, confirming that pressure can drive the phase transition just like temperature did. After removing the pressure, the spectrum returned to the original state (see R-0 and 0 in Figure 2g), validating the perfect reversibility of the SCO phase transition of **1** and the adjustability of the SCO transition via external pressure besides temperature, predicting considerable BCE in this complex.

Barocaloric Effect

By using the quasi-direct method,[9,11,13,20] the BCE of **1** was studied based on heat flow curves measured under external pressure up to 100 MPa (the upper limit of our P-DSC, Figure S3). Accordingly, the isothermal barocaloric entropy change ΔS_{iso} was obtained (Figure 3a) with the maximal ΔS_{iso} ~99 J K^{-1} kg^{-1} at a low pressure of 60 MPa for both compression and decompression. Then, the reversible ΔS_r by overlapping the area for heating and cooling of ΔS_{iso} is shown in Figure 3b. Even under a minuscule pressure of 20 MPa, a nonzero ΔS_r can be induced with a value of ~30 J K^{-1} kg^{-1}, which is appealing in terms of practical usage due to the high accessibility of such a low pressure. In addition, the maximal ΔS_r can reach 99 J K^{-1} kg^{-1} at 80 MPa with a half-height width of ~10 K (Figure S7). On this basis, a reversible refrigerant capacity (RC_{rev} = the maximal reversible entropy change × peak width at half height) of ~1000 J/kg at 100 MPa is obtained (Figure S7). Similarly, the adiabatic temperature change ΔT_{ad} was quasi-directly obtained, considering the contribution of specific heat capacity (Figure 3c, Figure S6). At a low pressure of 20 MPa, the ΔT_{ad} during compression and decompression is 2.4 and 2.3 K, respectively, rising to 14.2 and 12.2 K at 100 MPa. The reversible ΔT_r was determined as ±10.4 K under the application or removal of 100 MPa (Figure 3d). Moreover, taking into account the perfect linear relation of dT_C/dP (Figure S3b), BCE parameters under higher pressures above 100 MPa can be roughly evaluated, and the corresponding results were also plotted with dashed lines in Figure 3a−d. As pressure increases from 100 to 160 MPa, the half-height width of the ΔS_r peak broadens to 25 K, RC_{rev} doubles, and the maximal ΔT_r rises to 19 K.

We compared **1** (inorganic in nature) with some representative BCE peers, as illustrated in Figure 3e, where three essential factors are listed: maximal reversible $\Delta T_{r,max}$, maximal reversible $\Delta S_{r,max}$, and the barocaloric strength $\Delta S_{r,max}/P_{sat}$, where P_{sat} is the minimal pressure required to obtain $\Delta S_{r,max}$. One can see that, at a similar level in terms of these parameters, the required pressure for **1** (1 kbar) is less than half of those (all above 2 kbar) for the well-known plastic crystals NPA, AMP, and TRIS. Moreover, compared to inorganic categories, **1** occupies an absolutely superior position with $\Delta T_{r,max}$ being 2−3 times larger, $\Delta S_{r,max}$ being 1−2 times larger, and $\Delta S_{r,max}/P_{sat}$ being 2−3 times larger than those of the inorganic materials, even under a low pressure of 1 kbar. However, a common limitation across all materials is that their operating/cooling temperature range is seriously constrained by their own phase transition temperature T_C, which typically remains below 25 K even under 100 MPa pressure (Table 2). This makes it challenging to meet the demands of various cooling scenarios requiring a wide temperature span.

Table 2. Complexation Energy for Each H_2O and CH_3OH Solvent Molecule in the Crystalline Structure of 1 with Different Positions

1*H_2O (LS)	Complexation energy (eV)	1*CH_3OH (HS)	Complexation energy (eV)
H_2O 1	−0.16	CH_3OH 1	−0.40
H_2O 2	−0.29	CH_3OH 2	−0.39
H_2O 3	−0.29	CH_3OH 3	−0.41
H_2O 4	−0.16	CH_3OH 4	−0.43
H_2O 5	−0.29		
H_2O 6	−0.31		
overall	−2.78	overall	−3.00

T_C Adjustability and "Solvent-Caloric" Effect

Besides the BCE feasibility of **1**, more interesting is that the SCO transition T_C can be tuned by changing solvent environments. As shown in Figure 1, the CH_3OH and H_2O molecules can both enter the lattice of **1** through the channels along the *c*-axis, which alters the interaction surroundings microscopically via forming chemical bonds and hence changes the macroscopic physical properties of **1**. When the original **1** was exposed to CH_3OH atmosphere (Figure S9, Movie S2 and S3), it fast transformed into **1*CH$_3$OH** (Figure 4b) with the

Downloaded from pubs.acs.org/jacsat/article-pdf/148/33/35916/6653044/jacs.6c09635.pdf by INST OF PHYSICS user on 06 September 2026

https://doi.org/10.1021/jacs.6c09635
J. Am. Chem. Soc. 2026, 148, 35916−35928

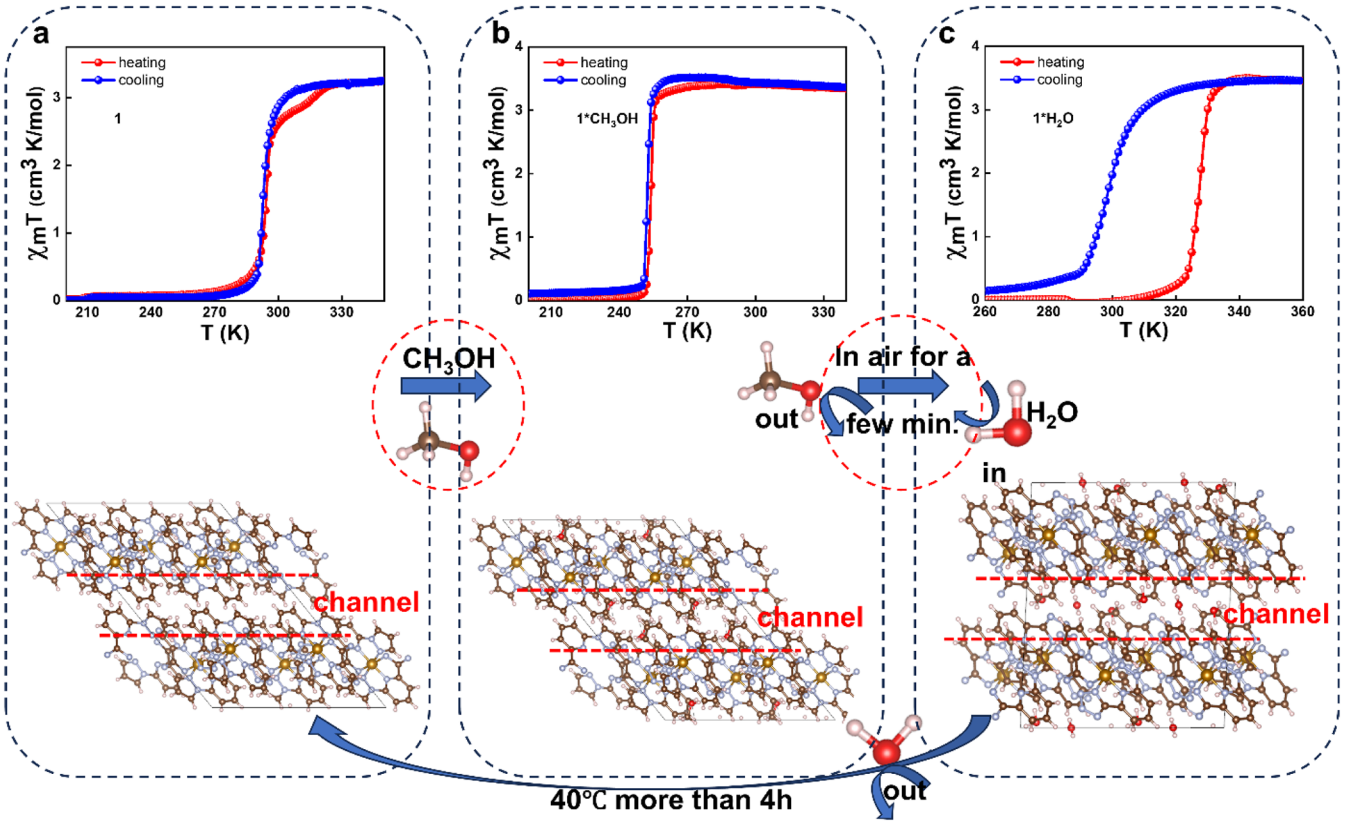


Figure 4. Adjustability of the SCO transition T_C. (a) The χ_mT-T plot of 1 without any solvents. (b) The χ_mT-T plot of 1*CH_3OH after the entrance of CH_3OH into the lattice. (c) The χ_mT-T plot of 1*H_2O after CH_3OH was replaced by H_2O, where the T_C during cooling is nonintrinsic, i.e., it is conspicuously different from the one during heating but approaches the one obtained in 1. This is because part of 1*H_2O transformed into 1 during heating due to the desorption of H_2O molecules, which is the same scenario described in Figure S11.

T_C shifting to a lower temperature of 250 K from the initial T_C ~ 295 K (Figure 4a). Then, if **1*CH_3OH** was placed in air for a few minutes, the CH_3OH would be replaced by H_2O and changed to **1*H_2O** with the T_C reversely shifting to a higher temperature of 330 K (Figure 4c). This transformation process is completely reversible; that is, **1*H_2O** soon transforms into **1*CH_3OH** when exposed to CH_3OH atmosphere (Figure S9, Movie S2 and S3), which changes back to the initial **1** if annealed at 40 °C in air.

To verify the amazing reversible process, we further performed cycled PXRD measurements (Figure 5a). First, the initial **1** without any solvents was recorded, which is the same as the one in Figure 2a for the LS. Next, CH_3OH liquid was dropped to **1** and data were collected after the yellow (**1*CH_3OH**) changed to red-orange (**1*H_2O**). One can note the appearance of the diagnostic diffraction peaks of **1*H_2O** at 8.19° and 26.48°, marked by "*". Further dropping CH_3OH makes the spectrum to change to another new form, with some peaks disappearing while new ones emerged, noting that "#" denotes the diagnostic peaks of **1*CH_3OH** at 12.77° and 25.78°. This process was repeated three times, and the reversibility was perfectly retained (Figure 5a; see details provided in the Methods section in the SI), which enables the occurrence of "solvent-caloric" effect.

Since there is a considerable gap between the T_C of **1*CH_3OH** (~250 K) and **1*H_2O** (~330 K), the spin state is likely to "commute" between LS and HS via CH_3OH/H_2O molecules, as denoted by the double arrow in Figure 5b, during which the driven enthalpy change and temperature change would occur due to the solvent in isothermal and adiabatic environments, respectively. This introduces a new concept in the refrigeration sector called "solvent-caloric" effect.

From the heat flow curves of **1*H_2O** and **1*CH_3OH** by DSC, the intrinsic entropy changes across T_C for **1*H_2O** and **1*CH_3OH** are around ~100 J K^{-1} kg^{-1} and ~120 J K^{-1} kg^{-1}, respectively (Figure 6a, b), a little higher than that of **1** without any solvent. This indicates that the introduction of solvent molecules not only shifted the T_C but also somewhat enlarged the latent heat of phase transition, probably because the differences in lattice distortion and the molecules/bonds vibration between HS and LS in **1*H_2O** and **1*CH_3OH** are likely more conspicuous compared with **1** itself, thus leading to a slightly larger entropy change considering that the spin nature is the same (S_{HS} = 2 and S_{LS} = 0) for the three forms (**1**, **1*H_2O** and **1*CH_3OH**). On this basis, the isothermal entropy change ΔS_{iso} and adiabatic temperature change ΔT_{ad} for the solvent-caloric effect were quasi-directly obtained (Figure 6c,d, Figure S11 and S12). One can see that the temperature window can be as wide as 80 K, from 240 to 320 K, driven by the commutation of H_2O and CH_3OH in the lattice, confirming the wide temperature span of this interesting caloric effect. In addition, the absolute values of ΔS_{iso} and ΔT_{ad} are also more than 100 J K^{-1} kg^{-1} and 25 K, respectively, which are significantly appealing in terms of cooling capacity (~9100 J/kg, more than 9 times that of **1** obtained via pressure at 100 MPa). All these results validate the high potential of this proposed "solvent-caloric" effect.

https://doi.org/10.1021/jacs.6c09635
J. Am. Chem. Soc. 2026, 148, 35916−35928

Downloaded from pubs.acs.org/jacsat/article-pdf/148/33/35916/6653044/jacs.6c09635.pdf by INST OF PHYSICS user on 06 September 2026

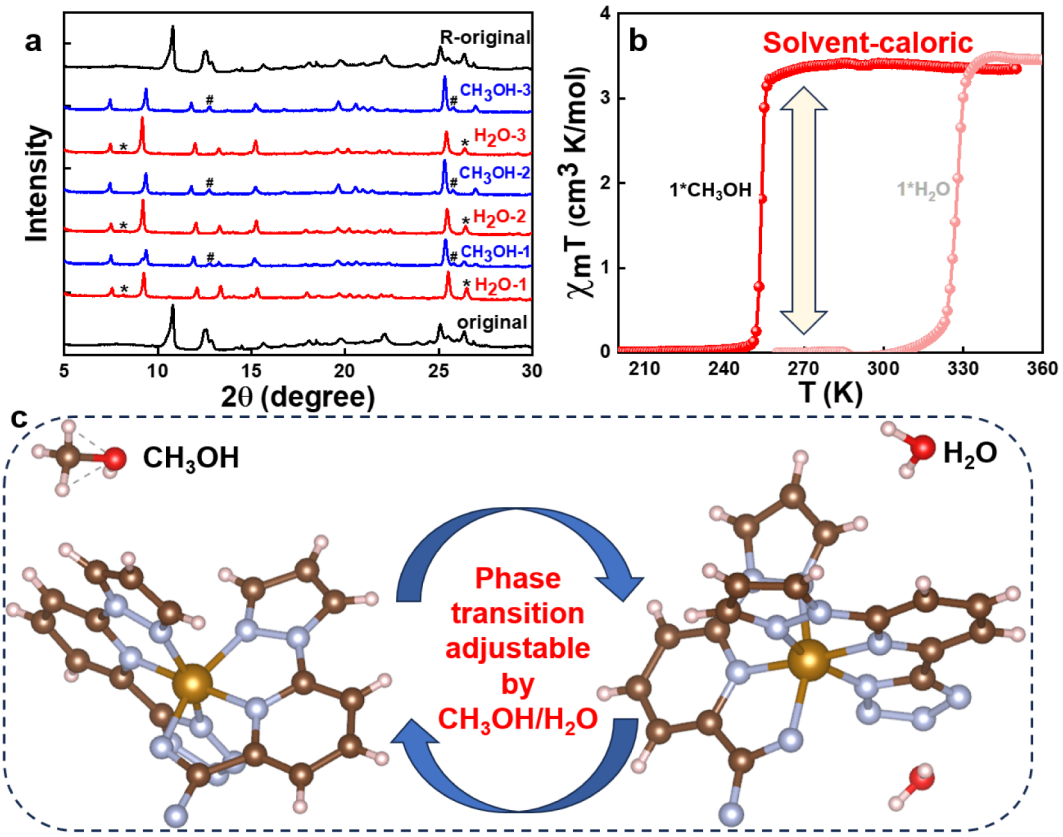


Figure 5. SCO transition driven by the commutation of CH_3OH and H_2O. (a) The cycled PXRD of repeated **1*H_2O** and **1*CH_3OH**. "*" and "#" denote the diagnostic peaks of **1*H_2O** and **1*CH_3OH**, respectively. (b) The LS-HS transition driven by the commutation of CH_3OH and H_2O. (c) An illustration diagram of the transition between **1*H_2O** and **1*CH_3OH** by the in-turn replacement of CH_3OH and H_2O in the lattice.

To further make sense, a solvent-driven Brayton thermodynamic refrigeration cycle was constructed, exactly analogous to the conventional gas-compression Brayton thermodynamic refrigeration cycle (see Supplementary Note S6). Subsequently, a quantitative comparison of thermodynamic terms between "solvent-caloric" and the BCE of sample **1** was conducted. Figure 6e presents the practical $S-T$ curve of the solvent-caloric effect upon guest molecule displacements between **1*CH_3OH** and **1*H_2O**, in comparison with the barocaloric effect of the parent sample **1** upon pressure change between 0.1 and 100 MPa (Figure 6f), wherein identical Brayton cycles are constructed. To quantitatively compare the refrigeration performance of the solvent-caloric effect and the barocaloric effect, the cooling load per cycle was set to be the same, $Q_c = \int_D^A T\mathrm{d}S$ (the heat absorbed at the cold end during the cycle), while the hot-end temperature of the solvent-caloric cycle was set at 315.0 K and that of the barocaloric cycle at 304.4 K. Subsequently, the input work $W = \oint T\mathrm{d}S$ (the area enclosed by the cycle) and the refrigeration temperature span, T_{span} (the difference between the hot-end and cold-end temperatures, $T_{span} = T_{hot\text{-}end} - T_{cold\text{-}end}$) can obtained (Table S7).

The results show that under nearly identical cooling loads (~14,900 J/kg), the solvent-caloric refrigeration achieves a temperature span (T_{soan}) per cycle as wide as 39.1 K—nearly four times that of the barocaloric cycle (11.3 K). Meanwhile, the required input work for the former (W_{sol} = 1385 J/kg) is about three times larger than that for the latter (W_{bar} = 451 J/kg). This indicates that, for the same cooling demand, the higher input work in the solvent-caloric cycle enables effective cooling over a much wider temperature range. However, it is worth noting that W_{sol} primarily originates from the chemical reaction potential during the spontaneous exchange of guest solvent molecules between 1·CH_3OH and 1·H_2O, rather than from external mechanical work. In other words, using guest-molecule displacement in place of pressure as the driving stimulus can similarly produce cooling and achieve superior performance.

Density Functional Theory (DFT) Calculations

To understand the conversion between **1*H_2O** and **1*CH_3OH**, DFT calculations were performed for the complexation energy between solvent molecules and Fe(II) complexes. On one hand, for H_2O-containing crystal, the complexation energy between 12 H_2O molecules and eight Fe(II) complexes in a unit cell (Figure 7a,c,e) was calculated to be −2.78 eV. Considering each H_2O molecule, the largest complexation energy is only −0.16 eV, and the smallest is −0.31 eV, as shown in Table 2. On the other hand, the total complexation energy between the 8 CH_3OH molecules and the eight Fe(II) complexes in CH_3OH-containing crystal (Figure 7b,d,f) was −3.00 eV, with the complexation energy for each CH_3OH ranging from −0.39 to −0.43 eV, a little smaller than that for H_2O-containing crystals (Table 2). These results are reasonable because CH_3OH molecule has a larger size than H_2O. Anyway, the complexation energy between either H_2O or CH_3OH molecule and the Fe(II) complex was not a large negative value, indicating that the interaction between the solvent and Fe complexes was not strong. The

Downloaded from pubs.acs.org/jacsat/article-pdf/148/33/35916/6653044/jacs.6c09635.pdf by INST OF PHYSICS user on 06 September 2026

https://doi.org/10.1021/jacs.6c09635
J. Am. Chem. Soc. 2026, 148, 35916−35928

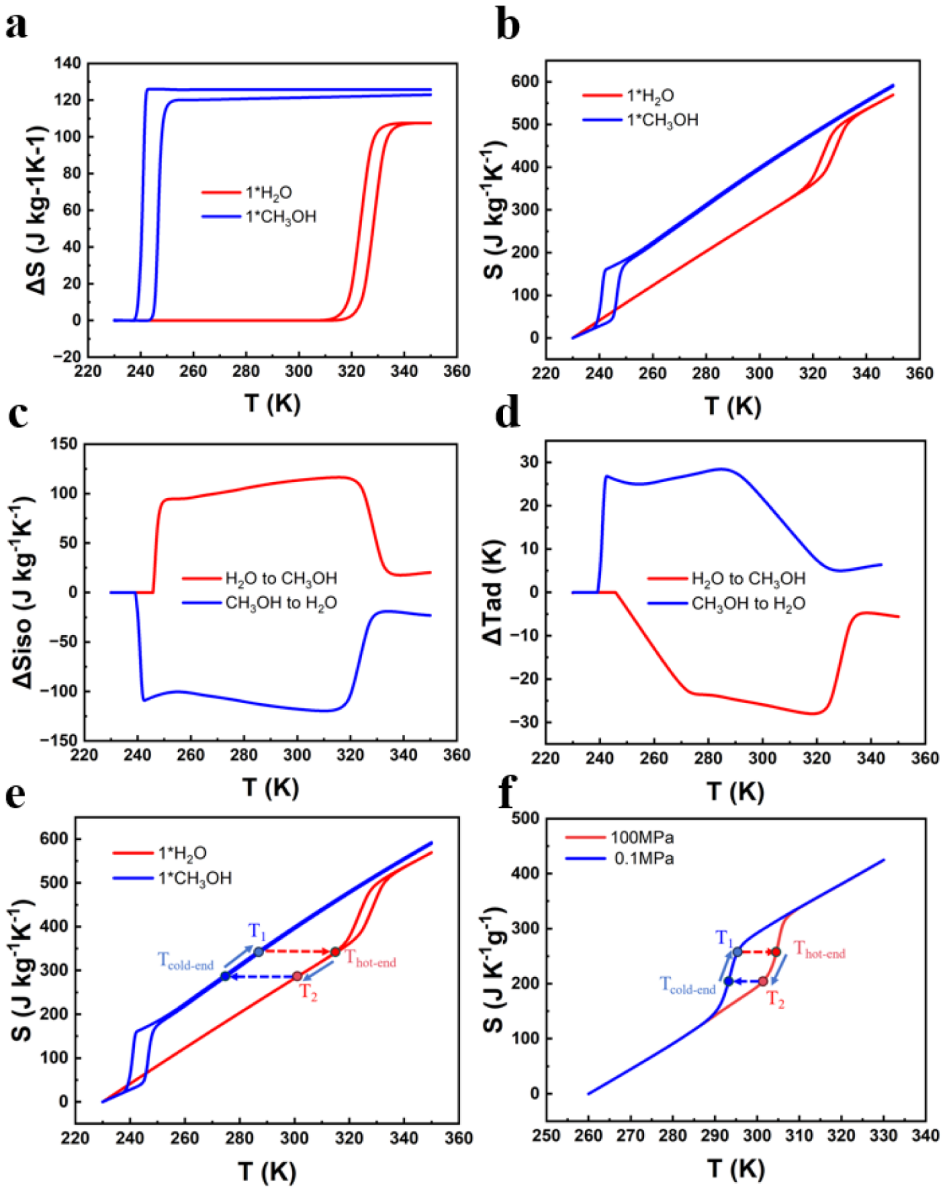


Figure 6. Solvent-caloric effect driven by the commutation of H_2O and CH_3OH molecules. (a) The entropy change across T_C for **1*H$_2$O** and **1*CH$_3$OH**. (b) The entropy after considering the heat capacity of **1*H$_2$O** and **1*CH$_3$OH** (Figure S26). (c) Entropy change ΔS_{iso} and (d) adiabatic temperature change ΔT_{ad} of the solvent-caloric effect. Brayton thermodynamic refrigeration cycle based on (e) solvent-caloric effect upon guest molecule displacements between **1*CH$_3$OH and 1*H$_2$O** and (f) barocaloric effect of parent sample **1** upon pressure change between 0.1 and 100 MPa.

accessible solvent surfaces for both crystals (Figure 7) clearly show interconnected channels along *c*-axis direction. However, the channels are separated in the *ab* plane and the CH_3OH-containing crystal has a larger free volume than H_2O-containing crystal, 27.93 Å^3 for H_2O vs 81.45 Å^3 for CH_3OH. These results indicate that solvent molecules (~1.232 Å in size for H_2O while ~1.306 Å for CH_3OH) can be adsorbed or removed via this channel along the *c*-axis easily; along with the small difference in the complexation energy for H_2O (−2.78 eV) and CH_3OH (−3.00 eV), the conversion between **1*H$_2$O** and **1*CH$_3$OH** happens straightforwardly.

DISCUSSION

In addition to the attractive BCE performance of sample **1**, an appealing characteristic is that its SCO transition temperature T_C can be shifted with the help of external solvents CH_3OH and H_2O, but without the need for pressure. In this work, the amounts of H_2O and CH_3OH molecules are 1.5 and 1 per unit cell of the original **1**, respectively, and a considerably large temperature span of ~80 K, from 240 to 320 K, was achieved, indicating that the cocrystallized guest molecules have an obvious influence on the spin crossover property of the host complex itself. Additionally, because of the weak combination energy of H_2O and CH_3OH molecules with **1**, these molecules can easily be replaced by each other if the chemical atmosphere overwhelms the old "resident" in the channel initially. Hence, "solvent-caloric" effect occurs. As for the transition speed between **1*H$_2$O** and **1*CH$_3$OH**, which is a critical parameter in terms of practical cooling applications, the concentration of the solvent atmosphere plays a key role. If methanol is directly dropped onto the sample, it transforms into **1*CH$_3$OH** within a few seconds (Movie S2), but when it is placed in a beaker

Downloaded from pubs.acs.org/jacsat/article-pdf/148/33/35916/6538044/jacs.6c09635.pdf by INST OF PHYSICS user on 06 September 2026

https://doi.org/10.1021/jacs.6c09635
J. Am. Chem. Soc. 2026, 148, 35916−35928

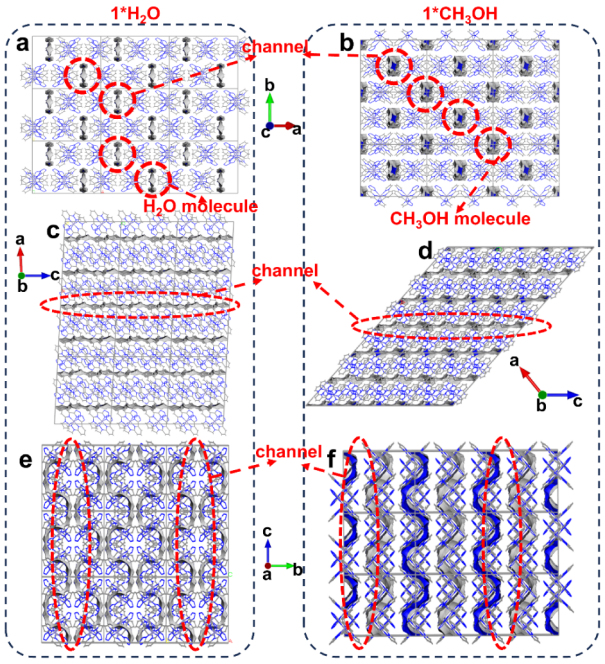


Figure 7. The accessible solvent surface channels for 1*H_2O and 1*CH_3OH. The view in the *ab* plane for (a) **1*H_2O** and (b) **1*CH_3OH**. Since the channels are along the *c*-axis, they are perpendicular to the screen in the *ab* plane as marked by the red dashed circles. The view in the *ac* plane for (c) **1*H_2O** and (d) **1*CH_3OH**. The view in the *bc* plane for (e) **1*H_2O** and (f) **1*CH_3OH**.

(Movie S3), it takes around 2 min to complete this transition. Therefore, to boost the transition speed in practice, the issue can be solved by increasing the specific concentration of solvent atmospheres. Moreover, upon carefully examining the structures reported here, one can find that the mononuclear complex can be constructed into a three-dimensional supramolecular network with the help of directional hydrogen bond interactions and/or $\pi\cdots\pi$ stacking, resulting in the formation of a regular channel, which can have a crucial influence on solvation or solvent exchange. Therefore, it is reasonably anticipated that other specific guest molecules with similar characteristics, like H_2O and CH_3OH can also be effective in tuning T_C, which can further enhance the versatility of the SCO system, as well as the solvent-caloric effect, due to the flexible tunability of T_C.

This interesting phenomenon can not only be used to detect the residual CH_3OH/H_2O in a certain surrounding based on its high sensitivity to the solvent atmosphere to **1** by observing the color of the sample as shown in Figure S9 and Movies S1 and S2. More importantly, it can also be leveraged to tune the spin state of **1**, i.e., transforming freely between LS and HS states by adjusting the solvent environment, as illustrated in Figure 6. From this, the refrigeration cycle can be controlled by solvent content in addition to pressure as a BCE candidate, and the possibility of a new concept in refrigeration based on solvent caloric may emerge. This concept deserves further exploration not only in **1** itself but also in other chemical complexes possessing similar traits sensitive to different solvents.

CONCLUSION

In summary, we report SCO complex **1** and its derivatives, which exhibit appealing caloric properties through the design of molecular channels, as confirmed by SC-XRD, P-DSC, PXRD, Raman, and DFT calculations. In addition to the colossal and reversible BCE observed in **1**, the existing molecular channels allow external solvent molecules (H_2O and CH_3OH) to enter or leave the lattice, significantly affecting the SCO transition properties and eventually leading to a tunable T_C and a broad refrigeration window of up to 80 K by simply altering the solvent atmosphere (which commonly requires ~400 MPa pressure for most BCE materials). Benefiting from the proposed "solvent-caloric" effect, RC can be increased more than 9-fold at ambient pressure compared to that achieved at 100 MPa in the same system using the conventional BCE method. Moreover, the constructed Brayton cycles indicate that, under nearly identical cooling loads, the solvent-caloric refrigeration achieves a temperature span nearly four times that of the barocaloric cycle, owing to the higher input work available from the chemical reaction potential. This work demonstrates that small external molecules residing in the SCO complex via molecular channels can cause a large impact on the phase transition characteristics, which can be utilized to orchestrate novel SCO materials with singular caloric performance. Our findings provide profound insight into the SCO series and offer constructive guidance for the development of sustainable, efficient, and universal cooling materials.

ASSOCIATED CONTENT

Supporting Information

The Supporting Information is available free of charge at https://pubs.acs.org/doi/10.1021/jacs.6c09635.

Illustration of the alternative adsorption of CH_3OH and H_2O in the lattice of 1 (MP4)

The color change of 1 when in contact with liquid methanal (MP4)

Direct record of the sensitivity to methanal atmosphere (MP4)

31 Supplementary Figures, 7 Supplementary Tables, and 7 Notes; additional experimental details, high-pressure differential calorimetry data, entropy curves used to evaluate barocaloric effects, PXRD data, single-crystal XRD data, views of the molecular channel from multiple directions, a solvent-driven Brayton thermodynamic refrigeration cycle, and direct measurements of isothermal entropy change in the solvent-caloric effect; full legends for Supplementary Movies S1−S3 (PDF)

Accession Codes

Deposition Numbers 2574641−2574643 contain the supplementary crystallographic data for this paper. These data can be obtained free of charge via the joint Cambridge Crystallographic Data Centre (CCDC) and Fachinformationszentrum Karlsruhe Access Structures service. www.ccdc.cam.ac.uk/data_request/cif

AUTHOR INFORMATION

Corresponding Authors

Feng-Xia Hu − *Beijing National Laboratory for Condensed Matter Physics, Institute of Physics, Chinese Academy of Sciences, Beijing 100190, P. R. China; School of Physical*

Downloaded from pubs.acs.org/jacsat/article-pdf/148/33/35916/6653044/jacs.6c09635.pdf by INST OF PHYSICS user on 06 September 2026

https://doi.org/10.1021/jacs.6c09635
J. Am. Chem. Soc. 2026, 148, 35916−35928

Sciences, University of Chinese Academy of Sciences, Beijing 101408, P. R. China; orcid.org/0000-0003-0383-0213; Email: fxhu@iphy.ac.cn

Bao-Gen Shen − *Beijing National Laboratory for Condensed Matter Physics, Institute of Physics, Chinese Academy of Sciences, Beijing 100190, P. R. China; School of Physical Sciences, University of Chinese Academy of Sciences, Beijing 101408, P. R. China; Ganjiang Innovation Academy, Chinese Academy of Sciences, Ganzhou, Jiangxi 341000, China; Ningbo Institute of Materials Technology & Engineering, Chinese Academy of Sciences, Ningbo, Zhejiang 315201, China;* orcid.org/0000-0003-4819-1806; Email: shenbg@iphy.ac.cn

Dao-Peng Zhang − *School of Chemistry and Chemical Engineering, Shandong University of Technology, Zibo 255049, P. R. China;* orcid.org/0000-0001-5653-7606; Email: dpzhang73@126.com

Authors

Yue Kan − *Beijing National Laboratory for Condensed Matter Physics, Institute of Physics, Chinese Academy of Sciences, Beijing 100190, P. R. China; School of Physical Sciences, University of Chinese Academy of Sciences, Beijing 101408, P. R. China*

Si-Wei Yan − *Beijing National Laboratory for Condensed Matter Physics, Institute of Physics, Chinese Academy of Sciences, Beijing 100190, P. R. China; School of Physical Sciences, University of Chinese Academy of Sciences, Beijing 101408, P. R. China*

Shuo Meng − *School of Chemistry and Chemical Engineering, Shandong University of Technology, Zibo 255049, P. R. China*

Yuan Lin − *Beijing National Laboratory for Condensed Matter Physics, Institute of Physics, Chinese Academy of Sciences, Beijing 100190, P. R. China; School of Physical Sciences, University of Chinese Academy of Sciences, Beijing 101408, P. R. China*

Rui-Xin Li − *School of Physics Science and Information Technology, Liaocheng University, Liaocheng 252000, China*

Qing-Zhen Huang − *Spallation Neutron Source Science Center, Dongguan 523803, P. R. China*

Yue-Xing Zhang − *Shandong Provincial Key Laboratory of Monocrystalline Silicon Semiconductor Materials and Technology, College of Chemistry and Chemical Engineering, Dezhou University, Dezhou 253023, P. R. China;* orcid.org/0000-0002-8510-5033

Zheng-Ying Tian − *Beijing National Laboratory for Condensed Matter Physics, Institute of Physics, Chinese Academy of Sciences, Beijing 100190, P. R. China; School of Physical Sciences, University of Chinese Academy of Sciences, Beijing 101408, P. R. China*

Jing Wang − *Beijing National Laboratory for Condensed Matter Physics, Institute of Physics, Chinese Academy of Sciences, Beijing 100190, P. R. China; School of Physical Sciences, University of Chinese Academy of Sciences, Beijing 101408, P. R. China;* orcid.org/0000-0001-5458-6711

Yuan-Sha Chen − *Beijing National Laboratory for Condensed Matter Physics, Institute of Physics, Chinese Academy of Sciences, Beijing 100190, P. R. China*

Yun-Zhong Chen − *Beijing National Laboratory for Condensed Matter Physics, Institute of Physics, Chinese Academy of Sciences, Beijing 100190, P. R. China;* orcid.org/0000-0001-8368-5823

Ji-Rong Sun − *Beijing National Laboratory for Condensed Matter Physics, Institute of Physics, Chinese Academy of Sciences, Beijing 100190, P. R. China;* orcid.org/0000-0003-4531-4794

Chang-Qing Jin − *Beijing National Laboratory for Condensed Matter Physics, Institute of Physics, Chinese Academy of Sciences, Beijing 100190, P. R. China; School of Physical Sciences, University of Chinese Academy of Sciences, Beijing 101408, P. R. China*

Complete contact information is available at: https://pubs.acs.org/10.1021/jacs.6c09635

Author Contributions

[##]Y.K., S.-W.Y., and S.M. contributed equally to this work.

Notes

The authors declare no competing financial interest.

■ ACKNOWLEDGMENTS

This work was supported by the National Key Research and Development Program of China (2023YFA1406003), the National Natural Science Foundation of China (52088101, 92263202, U23A20550, 12595332, 22171166, 22361132534, U25A6010), the Strategic Priority Research Program B (XDB1270201, XDB1720000) of the Chinese Academy of Sciences (CAS), the Synergetic Extreme Condition User Facility (SECUF), and the Shandong Provincial Key Laboratory of Monocrystalline Silicon Semiconductor Materials and Technology (2025KFKT033).

■ REFERENCES

(1) Stern, P. C.; Janda, K. B.; Brown, M. A.; Steg, L.; Vine, E. L.; Lutzenhiser, L. Opportunities and Insights for Reducing Fossil Fuel Consumption by Households and Organizations. *Nat. Energy* **2016**, *1* (5), 16043.

(2) Davis, L. W.; Gertler, P. J. Contribution of Air Conditioning Adoption to Future Energy Use under Global Warming. *Proc. Natl. Acad. Sci. U. S. A* **2015**, *112* (19), 5962−5967.

(3) Santamouris, M. Cooling the Buildings − Past, Present and Future. *Energy Build* **2016**, *128*, 617−638.

(4) McLinden, M. O.; Brown, J. S.; Brignoli, R.; Kazakov, A. F.; Domanski, P. A. Limited Options for Low-Global-Warming-Potential Refrigerants. *Nat. Commun* **2017**, *8* (1), 14476.

(5) Velders, G. J. M.; Fahey, D. W.; Daniel, J. S.; McFarland, M.; Andersen, S. O. The Large Contribution of Projected HFC Emissions to Future Climate Forcing. *Proc. Natl. Acad. Sci. U. S. A* **2009**, *106* (27), 10949−10954.

(6) Gao, Y.-H.; Wang, D.-H.; Hu, F.-X.; Huang, Q.-Z.; Song, Y.-T.; Yuan, S.-K.; Tian, Z.-Y.; Wang, B.-J.; Yu, Z.-B.; Zhou, H.-B.; Kan, Y.; Lin, Y.; Wang, J.; Li, Y.; Liu, Y.; Chen, Y.-Z.; Sun, J.-R.; Zhao, T.-Y.; Shen, B.-G. Low Pressure Reversibly Driving Colossal Barocaloric Effect in Two-Dimensional vdW Alkylammonium Halides. *Nat. Commun* **2024**, *15* (1), 1838.

(7) Lin, J.; Tong, P.; Zhang, K.; Tao, K.; Lu, W.; Wang, X.; Zhang, X.; Song, W.; Sun, Y. Colossal and Reversible Barocaloric Effect in Liquid-Solid-Transition Materials n-Alkanes. *Nat. Commun* **2022**, *13* (1), 596.

(8) Li, B.; Kawakita, Y.; Ohira-Kawamura, S.; Sugahara, T.; Wang, H.; Wang, J.; Chen, Y.; Kawaguchi, S. I.; Kawaguchi, S.; Ohara, K.; Li, K.; Yu, D.; Mole, R.; Hattori, T.; Kikuchi, T.; Yano, S.; Zhang, Z.; Zhang, Z.; Ren, W.; Lin, S.; Sakata, O.; Nakajima, K.; Zhang, Z. Colossal Barocaloric Effects in Plastic Crystals. *Nature* **2019**, *567* (7749), 506−510.

(9) Lloveras, P.; Aznar, A.; Barrio, M.; Negrier, P.; Popescu, C.; Planes, A.; Mañosa, L.; Stern-Taulats, E.; Avramenko, A.; Mathur, N. D.; Moya, X.; Tamarit, J.-L. Colossal Barocaloric Effects near Room

Downloaded from pubs.acs.org/jacsat/article-pdf/148/33/35916/6653044/jacs.6c09635.pdf by INST OF PHYSICS user on 06 September 2026

Temperature in Plastic Crystals of Neopentylglycol. *Nat. Commun* **2019**, *10* (1), 1803.
(10) Zhang, K.; Liu, Y.; Gao, Y.; Zhang, Z.; Wang, H.; Li, W.; Fan, X.; Ding, J.; Guan, Z.; Kawaguchi, S.; et al. Extreme Barocaloric Effect at Dissolution. *Nature* **2026**, *649*, 1180−1185.
(11) Kan, Y.; Hu, F.-X.; Wang, J.-T.; Hao, J.-Z.; Li, Q.; Cao, Y.-L.; Shen, F.-R.; Yin, W.; He, L.-H.; Su, B.; Wang, J.; Sun, J.-R.; Chen, Z.-G.; Jin, C.-Q.; Xing, X.-R.; Chen, Y.-Z.; Zhao, T.-Y.; Zhai, W.; Wei, B.-B.; Shen, B.-G. Colossal Barocaloric Effect in GdCl3-Doped H2O for Sustainable Cooling. *NPG Asia Mater* **2025**, *17* (1), 38.
(12) Sandeman, K. G. Research Update: The Mechanocaloric Potential of Spin Crossover Compounds. *APL Mater* **2016**, *4* (11), 111102.
(13) Romanini, M.; Wang, Y.; Gürpinar, K.; Ornelas, G.; Lloveras, P.; Zhang, Y.; Zheng, W.; Barrio, M.; Aznar, A.; Gràcia-Condal, A.; Emre, B.; Atakol, O.; Popescu, C.; Zhang, H.; Long, Y.; Balicas, L.; Lluís Tamarit, J.; Planes, A.; Shatruk, M.; Mañosa, L. Giant and Reversible Barocaloric Effect in Trinuclear Spin-Crossover Complex Fe3(Bntrz)6(Tcnset)6. *Adv. Mater* **2021**, *33* (10), 2008076.
(14) Vallone, S. P.; Tantillo, A. N.; dos Santos, A. M.; Molaison, J. J.; Kulmaczewski, R.; Chapoy, A.; Ahmadi, P.; Halcrow, M. A.; Sandeman, K. G. Giant Barocaloric Effect at the Spin Crossover Transition of a Molecular Crystal. *Adv. Mater* **2019**, *31* (23), 1807334.
(15) Ohkoshi, S.; Nakagawa, K.; Yoshikiyo, M.; Namai, A.; Imoto, K.; Nagane, Y.; Jia, F.; Stefanczyk, O.; Tokoro, H.; Wang, J.; Sugahara, T.; Chiba, K.; Motodohi, K.; Isogai, K.; Nishioka, K.; Momiki, T.; Hatano, R. Giant Adiabatic Temperature Change and Its Direct Measurement of a Barocaloric Effect in a Charge-Transfer Solid. *Nat. Commun* **2023**, *14* (1), 8466.
(16) Gütlich, P.; Goodwin, H. A. Spin Crossover—An Overall Perspective. In *Spin Crossover in Transition Metal Compounds I; Topics in Current Chemistry-Series*. Gutlich, P.; Goodwin, H. A., Eds.; Springer-Verlag: Berlin, 2004; Vol. *233*, pp. 1−47. .
(17) Real, J. A.; Gaspar, A. B.; Muñoz, M. C. Thermal, Pressure and Light Switchable Spin-Crossover Materials. *Dalton Trans* **2005**, *34* (12), 2062−2079.
(18) Schaefer, B.; Rajnak, C.; Salitros, I.; Fuhr, O.; Klar, D.; Schmitz-Antoniak, C.; Weschke, E.; Wende, H.; Ruben, M. Room Temperature Switching of a Neutral Molecular Iron(II) Complex. *Chem. Commun* **2013**, *49* (93), 10986−10988.
(19) Piper, S. L.; Melag, L.; Kar, M.; Sourjah, A.; Xiao, X.; May, E. F.; Aguey-Zinsou, K.-F.; MacFarlane, D. R.; Pringle, J. M. Organic Ionic Plastic Crystals Having Colossal Barocaloric Effects for Sustainable Refrigeration. *Science* **2025**, *387* (6729), 56−62.
(20) Seo, J.; Braun, J. D.; Dev, V. M.; Mason, J. A. Driving Barocaloric Effects in a Molecular Spin-Crossover Complex at Low Pressures. *J. Am. Chem. Soc* **2022**, *144* (14), 6493−6503.
(21) Seredyuk, M.; Li, R.; Znovjyak, K.; Zhang, Z.; Valverde-Muñoz, F. J.; Li, B.; Muñoz, M. C.; Li, Q.; Liu, B.; Levchenko, G.; Real, J. A. Reversible Colossal Barocaloric Effect of a New FeII Molecular Complex with Low Hysteretic Spin Crossover Behavior. *Adv. Funct. Mater* **2024**, *34* (30), 2315487.
(22) Yu, Z.; Zhou, H.; Hu, F.; Liu, C.; Yuan, S.; Wang, D.; Hao, J.; Gao, Y.; Wang, Y.; Wang, B.; Tian, Z.; Lin, Y.; Zhang, C.; Yin, Z.; Wang, J.; Chen, Y.; Li, Y.; Sun, J.; Zhao, T.; Shen, B. Colossal Barocaloric Effect Achieved by Exploiting the Amorphous High Entropy of Solidified Polyethylene Glycol. *NPG Asia Mater* **2022**, *14* (1), 96.
(23) Gao, Y.; Liu, H.; Hu, F.; Song, H.; Zhang, H.; Hao, J.; Liu, X.; Yu, Z.; Shen, F.; Wang, Y.; Zhou, H.; Wang, B.; Tian, Z.; Lin, Y.; Zhang, C.; Yin, Z.; Wang, J.; Chen, Y.; Li, Y.; Song, Y.; Shi, Y.; Zhao, T.; Sun, J.; Huang, Q.; Shen, B. Reversible Colossal Barocaloric Effect Dominated by Disordering of Organic Chains in $(CH_3{-}(CH_2)_{n-1}{-}NH_3)_2MnCl_4$ Single Crystals. *NPG Asia Mater* **2022**, *14* (1), 34.
(24) Fiaz, F.; Siddique, A.; Rabbee, M. F.; Bin Hanif, M.; Al-Baqami, S. M.; Jillani, S. M. S.; Almuqati, N. S.; Rahman, M. R.; Chowdhury, M. A.; Akhtar, M. N.; et al. Advances in Spin Crossover Metal Complexes: A Comprehensive Review on Its Gas Sensing Applications. *Rev. Inorg. Chem* **2026**, *46* (1), 35−59.
(25) Zhang, Y.; Torres-Cavanillas, R.; Yan, X.; Zeng, Y.; Jiang, M.; Clemente-Leon, M.; Coronado, E.; Shi, S. Spin Crossover Iron Complexes with Spin Transition near Room Temperature Based on Nitrogen Ligands Containing Aromatic Rings: From Molecular Design to Functional Devices. *Chem. Soc. Rev* **2024**, *53* (17), 8764−8789.
(26) Gentili, D.; Demitri, N.; Schäfer, B.; Liscio, F.; Bergenti, I.; Ruani, G.; Ruben, M.; Cavallini, M. Multi-Modal Sensing in Spin Crossover Compounds. *J. Mater. Chem. C* **2015**, *3* (30), 7836−7844.
(27) Piñeiro-López, L.; Valverde-Muñoz, F.-J.; Trzop, E.; Muñoz, M. C.; Seredyuk, M.; Castells-Gil, J.; Da Silva, I.; Martí-Gastaldo, C.; Collet, E.; Real, J. A. Guest Induced Reversible on−off Switching of Elastic Frustration in a 3D Spin Crossover Coordination Polymer with Room Temperature Hysteretic Behaviour. *Chem. Sci* **2021**, *12* (4), 1317−1326.
(28) Weber, B.; Bauer, W.; Pfaffeneder, T.; Dîrtu, M. M.; Naik, A. D.; Rotaru, A.; Garcia, Y. Influence of Hydrogen Bonding on the Hysteresis Width in Iron(II) Spin-Crossover Complexes. *Eur. J. Inorg. Chem* **2011**, *2011* (21), 3193−3206.
(29) Bushuev, M. B.; Lavrenova, L. G.; Ikorskii, V. N.; Shvedenkov, Y. G.; Varnek, V. A.; Sheludyakova, L. A.; Larionov, S. V. Iron(II) Complexes with 4-R-1,2,4-Triazoles (R = Ethyl, Propyl, Isopropyl): Synthesis and Properties. *Russ. J. Coord. Chem* **2004**, *30* (4), 284−290.
(30) Bushuev, M. B.; Pishchur, D. P.; Korolkov, I. V.; Vinogradova, K. A. Prototypical Iron(ii) Complex with 4-Amino-1,2,4-Triazole Reinvestigated: An Unexpected Impact of Water on Spin Transition. *Phys. Chem. Chem. Phys* **2017**, *19* (5), 4056−4068.
(31) Vieira, B. J. C.; Pereira, L. C. J.; Da Gama, V.; Waerenborgh, J. C. Structural Features That Modulate the Sharpness of the Spin Crossover Transition in $[Fe^{III}(5\text{-X-Qsal})_2]^+$ Based Salts. *CrystEngComm* **2023**, *25* (46), 6472−6477.
(32) Dîrtu, M. M.; Schmit, F.; Naik, A. D.; Rotaru, A.; Marchand-Brynaert, J.; Garcia, Y. Spin Transition Sensors Based on *β*-Amino-Acid 1,2,4-Triazole Derivative. *Int. J. Mol. Sci.* **2011**, *12* (8), 5339−5351.
(33) Roubeau, O.; Alcazar Gomez, J. M.; Balskus, E.; Kolnaar, J. J. A.; Haasnoot, J. G.; Reedijk, J. Spin-Transition Behaviour in Chains of Fe^{II} Bridged by 4-Substituted 1,2,4-Triazoles Carrying Alkyl Tails. *New J. Chem* **2001**, *25* (1), 144−150.
(34) Seredyuk, M.; Znovjyak, K.; Valverde-Muñoz, F. J.; Da Silva, I.; Muñoz, M. C.; Moroz, Y. S.; Real, J. A. 105 K Wide Room Temperature Spin Transition Memory Due to a Supramolecular Latch Mechanism. *J. Am. Chem. Soc* **2022**, *144* (31), 14297−14309.
(35) Zhang, L.; Xu, G.-C.; Xu, H.-B.; Zhang, T.; Wang, Z.-M.; Yuan, M.; Gao, S. Abrupt Spin Transition around Room Temperature and Light Induced Properties in Fe^{II} Complexes with N_4O_2 Coordination Sphere. *Chem. Commun* **2010**, *46* (15), 2554.
(36) Senthil Kumar, K.; Vela, S.; Heinrich, B.; Suryadevara, N.; Karmazin, L.; Bailly, C.; Ruben, M. Bi-Stable Spin-Crossover in Charge-Neutral $[Fe(R\text{-}Ptp)_2]$ (Ptp = 2-(1*H*-Pyrazol-1-Yl)-6-(1*H*-Tetrazol-5-Yl)Pyridine) Complexes. *Dalton Trans* **2020**, *49* (4), 1022−1031.
(37) Molnár, G.; Niel, V.; Gaspar, A. B.; Real, J.-A.; Zwick, A.; Bousseksou, A.; McGarvey, J. J. Vibrational Spectroscopy of Cyanide-Bridged, Iron(II) Spin-Crossover Coordination Polymers: Estimation of Vibrational Contributions to the Entropy Change Associated with the Spin Transition. *J. Phys. Chem. B* **2002**, *106* (38), 9701−9707.
(38) Molnár, G.; Kitazawa, T.; Dubrovinsky, L.; McGarvey, J. J.; Bousseksou, A. Pressure Tuning Raman Spectroscopy of the Spin Crossover Coordination Polymer $Fe(C_5H_5N)_2[Ni(CN)_4]$. *J. Phys.: Condens. Matter* **2004**, *16* (14), S1129−S1136.
(39) Molnár, G.; Bousseksou, A.; Zwick, A.; McGarvey, J. J. The Spin-Crossover Phenomenon in the Solid State: Do Domains Play a Role? A Micro-Raman Study. *Chem. Phys. Lett* **2003**, *367* (5−6), 593−598.

Downloaded from pubs.acs.org/jacsat/article-pdf/148/33/35916/6653044/jacs.6c09635.pdf by INST OF PHYSICS user on 06 September 2026

https://doi.org/10.1021/jacs.6c09635
J. Am. Chem. Soc. 2026, 148, 35916−35928

(40) Reis, M.; Cheng, Y.; dos Santos, A. M. Spin Crossover Transition Driven by Pressure: Barocaloric Applications. *Phys. B* **2024**, *677*, 415689.
(41) Bousseksou, A.; McGarvey, J. J.; Varret, F.; Real, J. A.; Tuchagues, J. P.; Dennis, A. C.; Boillot, M. L. Raman Spectroscopy of the High- and Low-Spin States of the Spin Crossover Complex Fe(Phen)2(NCS)2: An Initial Approach to Estimation of Vibrational Contributions to the Associated Entropy Change. *Chem. Phys. Lett* **2000**, *318* (4−5), 409−416.
(42) D'Avino, G.; Painelli, A.; Boukheddaden, K. Vibronic Model for Spin Crossover Complexes. *Phys. Rev. B* **2011**, *84* (10), 104119.
(43) Vela, S.; Ribas-Arino, J.; Vallone, S. P.; dos Santos, A. M.; Halcrow, M. A.; Sandeman, K. G. Atomistic Description of Spin Crossover under Pressure and Its Giant Barocaloric Effect. *J. Mater. Chem. C* **2025**, *13* (38), 19635−19641.
(44) Aznar, A.; Lloveras, P.; Barrio, M.; Negrier, P.; Planes, A.; Mañosa, L.; Mathur, N. D.; Moya, X.; Tamarit, J.-L. Reversible and Irreversible Colossal Barocaloric Effects in Plastic Crystals. *J. Mater. Chem. A* **2020**, *8* (2), 639−647.
(45) Bermúdez-García, J. M.; Sánchez-Andújar, M.; Castro-García, S.; López-Beceiro, J.; Artiaga, R.; Señarís-Rodríguez, M. A. Giant Barocaloric Effect in the Ferroic Organic-Inorganic Hybrid [TPrA]-[$Mn(Dca)_3$] Perovskite under Easily Accessible Pressures. *Nat. Commun* **2017**, *8* (1), 15715.
(46) Salvatori, A.; Aguilà, D.; Aromí, G.; Mañosa, L.; Planes, A.; Lloveras, P.; Pardo, L. C.; Appel, M.; Nataf, G. F.; Giovannelli, F.; Barrio, M.; Tamarit, J. L.; Romanini, M. Large Barocaloric Effects in Two Novel Ferroelectric Molecular Plastic Crystals. *J. Mater. Chem. A* **2023**, *11* (23), 12140−12150.
(47) García-Ben, J.; Delgado-Ferreiro, I.; Dixey, R. J. C.; Castro-García, S.; López-Beceiro, J.; Artiaga, R.; Sánchez-Andújar, M.; Phillips, A. E.; Bermúdez-García, J. M.; Señarís-Rodríguez, M. A. Unveiling Barocaloric Potential in Organometallic-Sandwich Compounds [Cp_2M][PF_6] (M: Fe^{3+}, Co^{3+}). *J. Mater. Chem. A* **2024**, *12* (35), 23751−23760.
(48) Aznar, A.; Lloveras, P.; Kim, J.; Stern-Taulats, E.; Barrio, M.; Tamarit, J. L.; Sánchez-Valdés, C. F.; Sánchez Llamazares, J. L.; Mathur, N. D.; Moya, X. Giant and Reversible Inverse Barocaloric Effects near Room Temperature in Ferromagnetic $MnCoGeB_{0.03}$. *Adv. Mater* **2019**, *31* (37), 1903577.
(49) Aznar, A.; Lloveras, P.; Romanini, M.; Barrio, M.; Tamarit, J.-L.; Cazorla, C.; Errandonea, D.; Mathur, N. D.; Planes, A.; Moya, X.; Mañosa, L. Giant Barocaloric Effects over a Wide Temperature Range in Superionic Conductor AgI. *Nat. Commun* **2017**, *8* (1), 1851.
(50) Lloveras, P.; Stern-Taulats, E.; Barrio, M.; Tamarit, J.-L.; Crossley, S.; Li, W.; Pomjakushin, V.; Planes, A.; Mañosa, L.; Mathur, N. D.; Moya, X. Giant Barocaloric Effects at Low Pressure in Ferrielectric Ammonium Sulphate. *Nat. Commun* **2015**, *6* (1), 8801.
(51) Li, J.; Dunstan, D.; Lou, X.; Planes, A.; Mañosa, L.; Barrio, M.; Tamarit, J.-L.; Lloveras, P. Reversible Barocaloric Effects over a Large Temperature Span in Fullerite C_{60}. *J. Mater. Chem. A* **2020**, *8* (39), 20354−20362.
(52) Zhang, K.; Song, R.; Qi, J.; Zhang, Z.; Zhang, Z.; Yu, C.; Li, K.; Zhang, Z.; Li, B. Colossal Barocaloric Effect in Carboranes as a Performance Tradeoff. *Adv. Funct. Mater* **2022**, *32* (20), 2112622.
(53) Ren, Q.; Qi, J.; Yu, D.; Zhang, Z.; Song, R.; Song, W.; Yuan, B.; Wang, T.; Ren, W.; Zhang, Z.; Tong, X.; Li, B. Ultrasensitive Barocaloric Material for Room-Temperature Solid-State Refrigeration. *Nat. Commun* **2022**, *13* (1), 2293.

Downloaded from pubs.acs.org/jacsat/article-pdf/148/33/35916/6538044/jacs.6c09635.pdf by INST OF PHYSICS user on 06 September 2026

https://doi.org/10.1021/jacs.6c09635
J. Am. Chem. Soc. 2026, 148, 35916−35928